Coexistence of electron and phonon topology in conjunction with quantum transport device modeling

IOP Publishing Journal of Physics: Condensed Matter
J. Phys.: Condens. Matter **36** (2024) 155501 (13pp) https://doi.org/10.1088/1361-648X/ad1a5b

Coexistence of electron and phonon topology in conjunction with quantum transport device modeling

Anusree C V, Sonali S Pradhan and V Kanchana*

Department of Physics, Indian Institute of Technology Hyderabad, Kandi, Medak 502 284, Telangana, India

E-mail: kanchana@phy.iith.ac.in

Received 1 November 2023, revised 15 December 2023
Accepted for publication 3 January 2024
Published 19 January 2024

Abstract

The escalating research in the field of topology necessitates an understanding of the underlying rich physics behind the materials possessing unique features of non-trivial topology in both electronic and phononic states. Due to the interaction between electronic quasiparticles and spin degrees of freedom, the realization of magnetic topological materials has opened up a new frontier with unusual topological phases, however, these are rarely reported alongside phononic quasiparticle excitations. In this work, by first-principles calculations and symmetry analysis, the intermetallic ferromagnetic compounds MnGaGe and MnZnSb with the coexistence of exceptional topological features in the electronic and phononic states are proposed. These compounds host nodal surface on $k_y = \pi$ plane in bulk Brillouin zone in the electronic and phononic spectra protected by the combination of time-reversal symmetry and nonsymmorphic two-fold screw-rotation symmetry. In the former case, a spin-polarized nodal surface is present in the majority and minority spin channels and found to be robust to ground-state magnetic polarization. The presence of nodal line features is analyzed in both the quasiparticle spectra, whose non-trivial nature is confirmed by the Berry phase calculation. The incorporation of spin–orbit coupling in the electron spectra introduces distinctive characteristics in the transport properties, facilitating the emergence of anomalous Hall conductivity through Berry curvature in both bulk and monolayer. Furthermore, the monolayer has been proposed as a two-terminal device model to investigate the quantum transport properties using the non-equilibrium Green's function approach. This superlative combination of observations and modeling sets the path for a greater level of insight into the behavior and aspects of topological materials at the atomic scale.

Supplementary material for this article is available online

Keywords: magnetism, electron topology, phonon topology, quantum transport

1. Introduction

The emergence of topological insulators has ignited an exceptional surge of research interest in condensed matter physics and materials science. The captivating domain of topological states of matter continues to intrigue owing to its profound potential and far-reaching implications [1]. In recent years, increased attention has been devoted to the exploration of topological semimetals (TSMs) and metals, further enriching our understanding of these remarkable states of matter [2, 3]. Based on the number of band degeneracy in their first Brillouin zone (BZ), TSMs are further divided into three distinct types: Weyl, with isolated Weyl points [4, 5], Dirac, with

* Author to whom any correspondence should be addressed.

a Dirac node [6, 7], and topological nodal line [8–11] hosting a continuous line of node or ring or even higher-order band degeneracy [12–14]. Furthermore, TSMs can be classified into nodal points, having zero-dimension band crossing like carbon-based topological materials [15, 16], nodal line, having one-dimensional band crossing along a specific line [17, 18].

The topological characteristics of the electronic states have garnered substantial attention and have been the subject of extensive research because of their diverse range of physical mechanisms. Recently, this interest has experienced a resurgence with the exploration of topological phonons, which are quantized vibrational states in interacting lattices protected by symmetry [19–21]. This is because topological phonons, which exhibit little or no scattering in their transport processes, can provide extra advantages for being unconstrained by the Fermi level (E_F). It is feasible to observe and characterize the topological features of phonons over a broad frequency range because they are not susceptible to the Pauli exclusion principle, which makes them the main emergent type of boson-like quasiparticles. Owing to this distinctive property, a variety of topological phonons have recently been discovered, including the Weyl phonons [22, 23], Dirac phonons [24, 25], double-Weyl phonons [26, 27], hourglass phonons [22, 28], nodal surface phonons [29–31] and the nodal line phonons [32, 33].

Nodal surface semimetals/metals are a class of materials defined by band degeneracy on closed nodal surfaces within the BZ, shielded by crystalline symmetries. These electronic states were first mentioned by Zhong *et al* [34] and Liang *et al* [35] in carbon networks and the $BaVS_3$ family of materials. Later on, Wu *et al* [36] proposed necessary conditions and illustrations for robust nodal surface in magnetic materials and even in the presence of spin–orbit coupling (SOC). More notable research works that have explored the properties of non-magnetic (NM) compounds include K_6YO_4 [36], Sr_5X_3 [37] and Ti_3Al [38], while the investigations on the magnetic compounds incorporated XYZ_3 (X = Cs, Rb, Y = Cr, Cu, Z = Cl, I) [39] and $XTiO_2$ (X = Li, Na, K, Rb) [40]. Phononic nodal surfaces have also been studied in NM cases [29–33], but seldom seen in magnetic ones. However, it is rare to witness both types of nodal surface together in a compound.

Topological materials offer high efficiency and low power consumption in electrical conduction [41, 42], along with resistance against impurity-induced scattering. These characteristics render them highly beneficial for nanoscale devices. A significant subset within this domain is magnetic TSMs, which play a crucial role in spintronics by amalgamating topology, quantum transport, and magnetism. Unlike NM counterparts that rely on time-reversal symmetry, magnetic TSMs derive their topological states from adaptable symmetries affected by the direction of magnetization. This has spurred a burgeoning interest in investigating topological states within magnetic systems, illustrated by materials such as MnAlGe [43], Co_2S_2TI [44], CuMnAs [45], and Co-based Heusler alloys [46, 47].

Monolayer devices represent an enticing frontier in advanced technology, where material properties in a single layer offer a glimpse of a future where science and innovation seamlessly merge [48, 49]. Graphene monolayers, known for their remarkable conductivity, endow electrons with high mobility, ballistic transport, and unique quantum Hall effects [50]. Monolayer semiconductors, with direct bandgaps and strong light–matter interactions, hold great promise for the next generation of flexible electronics and optoelectronics [51]. Additionally, the exceptional spin transport properties and extended spin lifetimes of two-dimensional (2D) materials provide an exquisite platform for manipulating electron spins, positioning them as leading contenders in advanced spintronics applications [52, 53].

In this paper, by first-principles calculations, we focus on the Cu_2Sb-type layered intermetallic magnetic compounds MnGaGe and MnZnSb for elucidating the unexplored coexistence of the topological characteristics within their electronic and phononic band structures. In the electronic and phononic spectra of the investigated compounds, the combination of time-reversal symmetry and nonsymmorphic two-fold screw-rotation symmetry preserves the nodal surface on $k_y = \pm\pi$ plane. Both the majority and minority spin channels in the electron spectra exhibit nodal surface and are robust to SOC along the ground-state magnetization. In addition to this, nodal line features are also investigated in both the quasiparticle spectra. In the case of electron spectra, SOC effects on the nodal crossings are discussed and thereby computed anomalous Hall conductivity (AHC). As a result, our findings allude to a plausible material framework for investigating aspects of various topological states. Furthermore, the layering possibility has been explored accompanied by the novel application of quantum transport device modeling.

2. Computational details

The investigated compounds underwent full geometry optimization using first-principles calculations implemented in the *Vienna ab initio simulation package* [54]. The calculations employed the projector augmented wave [55] method with generalized gradient approximation (GGA) [56] and Perdew–Burke–Ernzerhof (PBE) functions to determine the ionic potential and exchange-correlation interaction. A plane wave cutoff energy of 500 eV and a Γ-centered k-mesh of $10 \times 10 \times 8$ for bulk and $10 \times 10 \times 1$ for monolayer were used for self-consistent calculations in such a way that the energy and force were converged up to 10^{-6} eV and 10^{-2} eV Å^{-1} respectively. Phonon dispersion was calculated using the density functional perturbation approach with PHONOPY [57]. To assess the topological nature, a tight-binding Hamiltonian was generated using maximally localized Wannier functions (MLWFs) [58, 59] and an iterative Green's function method with WANNIER90 [60] package. Berry curvature (BC), Ω was calculated through Kubo formalism [61, 62], surface state properties and AHC were computed using the WANNIERTOOLS [63] package.

The quantum transport properties were evaluated through the use of density functional theory (DFT) with SIESTA [64] and the non-equilibrium Green's function method as implemented in GOLLUM-2.0 [65]. The computational approach adopted

by SIESTA involves employing a localized numerical-atomic orbital basis set. A single-polarization basis set, PBE–GGA exchange-correlation functional with a cutoff energy of 600 Ry and an energy shift of 0.001 Ry was applied. Transverse directions are subject to periodic boundary conditions, and transport computations are performed along the edges of interest in the semi-infinite direction. The Monkhorst–Pack grid with a dense $1 \times 1 \times 10$ k-point grid generates the Hamiltonian. The Landauer method is then used to compute the electric current (I), which can be found by integrating the transmission curve [66]

$$I = \frac{2e^2}{h} \int_{-\infty}^{\infty} T(E)\,[f_{\mathrm{R}}(E) - f_{\mathrm{L}}(E)]\,\mathrm{d}E, \tag{1}$$

where I represents the electric current under applied bias voltage, e is the electric charge, h is the planks constant, $f_{\mathrm{R}}(E)$ and $f_{\mathrm{L}}(E)$ is the Fermi–Dirac distribution function of the right and left electrode. The DFT calculations yield the Hamiltonian, H, and overlap matrices, S, which are used to calculate the electron transmission coefficient, $T(E)$, representing the likelihood of electrons passing through a device between left and right electrodes at a given energy level, E. $T(E)$ is calculated using the retarded Green's function, $G(E)$, determined by the equation $G = (ES - H - \Sigma_{\mathrm{L}} - \Sigma_{\mathrm{R}})^{-1}$, where Σ_{L} and Σ_{R} are self-energy terms describing the interaction between the electrodes and the device. The level broadening, Γ, is given by $\Gamma = i[\Sigma(E) - \Sigma^{\dagger}(E)]$. $T(E)$ is obtained using the equation $T(E) = \mathrm{Tr}[\Gamma_{\mathrm{R}}(E)G(E)\Gamma_{\mathrm{L}}(E)G^{\dagger}(E)]$, where Tr is the trace function, considering the level broadening and the probability of electron transmission between the electrodes due to the interaction with the device [66].

3. Crystal structure and magnetic properties

The intermetallic compounds MnGaGe and MnZnSb crystallize in the tetragonal Cu_2Sb-type layered structure with space group $P4/nmm$ (129). These compounds are known for their significant magnetic anisotropy, closely related to their anisotropic crystal structure [68]. The Mn atoms form square-net layers perpendicular to the c-axis, with larger distances between adjacent net planes compared to the spacing between the nearest Mn atoms in the net plane as shown in figure 1(a), giving rise to a quasi-2D structure [67, 69]. Each unit cell comprises six atoms with Mn atoms at positions 2a (0, 0, 0) and (1, 1, 0), Y atoms at positions 2c (0, 1/2, 0.273) and (0, 1/2, $\overline{0.273}$), and Z atoms at positions (0, 1/2, 0.720) and (0, 1/2, $\overline{0.720}$). In the crystal structure, the Mn layers are separated by NM Y/Z layers. Each Mn atom is tetrahedrally coordinated to four equidistant Z atoms, forming linear chains of a tetrahedral configuration (MnZ_4), with Y atoms spacing them along the c-axis as illustrated in figure 1(b). The corresponding bulk BZ along the high symmetry points depicting the nodal surface with the shaded region is shown in figure 1(c). The optimized parameters of the structure are in accordance with the experimental data as summarized in table 1. These compounds

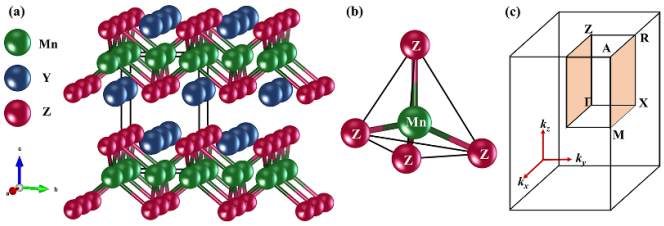

Figure 1. (a) The crystal structure of MnYZ (Y = Ga/Zn and Z = Ge/Sb). (b) The depiction of tetrahedral coordination of Mn by Z atoms (MnZ_4). (c) The bulk BZ with the shaded region exhibits the presence of nodal surface.

Table 1. The experimental and optimized parameters of the compounds.

	Experimental [67]		Optimized	
Compound	$a = b$ (Å)	c (Å)	$a = b$ (Å)	c (Å)
MnGaGe	3.971	5.873	3.944	5.893
MnZnSb	4.173	6.233	4.147	6.240

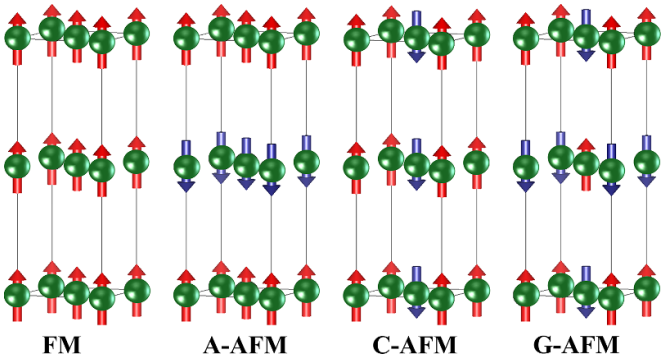

Figure 2. The schematic representation of the spin alignment of Mn atoms in various configurations using $1 \times 1 \times 2$ supercell.

possess inversion symmetry and nonsymmorphic space group symmetry (glide mirror and two-fold screw rotation).

The ground state of these compounds was determined theoretically by considering different magnetic spin configurations, including ferromagnetic (FM), antiferromagnetic (A-AFM, C-AFM, and G-AFM), and NM, using $1 \times 1 \times 2$ supercell as illustrated in figure 2. The most stable configuration was found to be FM, with the lowest energy. The DFT + SOC approach was applied to identify the preferred magnetization direction, which was determined to be [001]. Therefore, the magnetic ground state of these compounds features FM ordering, with Mn atoms magnetized along the z direction. The computed total energies of the compounds per unit cell under various magnetic configurations are encapsulated in table 2.

Experimental findings indicate that these compounds exhibit significant anisotropic magnetism along the c-axis and are ferromagnetically ordered with Curie temperatures (T_c) of 453 K for MnGaGe and 320 K for MnZnSb [67, 69–71]. The experimental magnetic moments of Mn atoms were reported to be 1.65 μ_{B} and 1.5 μ_{B} for MnGaGe and MnZnSb

Table 2. Total energy (E_{tot}) of the compounds per unit cell (in meV) under various magnetic configurations with reference to $FM_{[001]}$.

Compound	Parameter	$FM_{[001]}$	$FM_{[100]}$	$FM_{[010]}$	A-AFM	C-AFM	G-AFM	NM
MnGaGe	E_{tot}	0	0.233	0.232	111.379	233.067	332.378	830.598
MnZnSb	E_{tot}	0	0.196	0.197	175.962	209.988	289.884	1326.801

[67], respectively, while theoretical observations suggest values of 2.24 μ_B and 2.59 μ_B. These compounds share similar crystal structures and magnetic properties. Therefore, MnGaGe serves as illustrative material for exploring topological electronic and phononic characteristics and quantum transport device modeling in monolayer. The detailed results for MnZnSb can be found in the supplemental material accompanying this study.

4. Electronic band structure

The spin-polarized band structure of the optimized magnetic ground state of MnGaGe with and without the inclusion of SOC with magnetization along z-direction is shown in figure 3(a). This compound is metallic with spin-up and spin-down channels resembling the same. The density of states (DOS) plot given in figure 3(b) exemplifies that Mn-d orbitals make up the majority of the contribution.

The band dispersion along X–M and R–A is found to be doubly degenerate along spin-up and spin-down channels and remains the same with ground state magnetization direction [001], as depicted in figure 3(a) using the shaded regions. These doubly degenerate band crossings form a 2D surface along the k path X–M–A–R–X ($k_y = \pi$ plane), such that each point on the surface is a crossing between two bands whose dispersion is normal to the surface. Nodal line features are analyzed, and Berry phase calculations are done to confirm their non-trivial nature. The inclusion of SOC leads to the formation of four pairs of Weyl nodes in the BZ, which act as the source and sink of significant Berry flux and are known to have intriguing transport characteristics, providing an ideal framework for achieving a BC induced AHC. These are the glimpses of the topological features present in the electronic band structure of MnGaGe which will be discussed in detail in the subsequent sections.

4.1. Spin-polarized nodal surface and magnetization

Let us now look at the doubly degenerate band dispersion along X–M and R–A, which forms a 2D surface along the k-path X–M–A–R–X, which lies on the $k_y = \pi$ plane in the BZ. It is intriguing to observe that the band degeneracy extends the entire plane and generates a nodal surface in both spin channels. As this compound crystallizes in the $P4/nmm$ space group, the combination of non-symmorphic two-fold screw-rotational symmetry ($\mathcal{S}_{2i}$) and time-reversal symmetry ($\mathcal{T}$) ensures the class II type of nodal surface [36].

In the absence of SOC, each spin channel can be regarded as a spinless system because spin and orbital degrees of freedom are independent. So, it is found that $(\mathcal{S}_{2y})^2 = T_{010} = e^{-ik_y}$, where T_{010} is the translation of a lattice constant in the y direction. The antiunitary operator $\mathcal{T}\mathcal{S}_{2y}$, which combines $\mathcal{S}_{2y}$ and $\mathcal{T}$, can only inverse k_y since $\mathcal{T}$ is antiunitary and inverts momentum space with the relation $\mathcal{T}^2 = 1$. The Kramer-like degeneracy on the $k_y = \pi$ plane is shown by the fact that $(\mathcal{T}\mathcal{S}_{2y})^2 = T_{010} = e^{-ik_y}\,|_{k_y=\pi} = -1$. To better comprehend the nodal surface existence, band dispersions along the symmetry pathways depicted in figure 4(a) are computed for both the spin channels as shown in figures 4(b)–(f) and (g)–(k). Every point on the $k_y = \pi$ plane exhibits two-fold Kramer's degeneracy, which leads to the generation of the nodal surface via the combined symmetry $\mathcal{T}\mathcal{S}_{2y}$ even while the individual $\mathcal{T}$ or $\mathcal{S}_{2y}$ is broken [36].

Considering the presence of SOC, where spin and orbital degrees of freedom are intertwined, the symmetry operations affect both spin and orbitals simultaneously. In this context, the nodal surface will exist only if the composite symmetry $\mathcal{T}\mathcal{S}_{2y}$ is preserved. When the magnetic moments align perpendicular to the screw axis, the composite symmetry is maintained. Conversely, when the magnetic moments align parallel to the screw axis, the composite symmetry is broken. The band dispersion along the k-path Γ–X–M–A–R–X for various magnetization directions is depicted in figures 5(a)–(c). It is observed that the nodal surface is preserved along [001] and [100] directions as they are perpendicular to the screw axis, while it is broken (degeneracy lifted) along the [010] direction since it is parallel to the screw axis. For MnGaGe, the ground state magnetization is along the [001] direction, which preserves nodal surface on the $k_y = \pi$ plane as illustrated in figures 5(d)–(h).

It is viable for multiple nodal surfaces to exist, either equivalent or inequivalent if the space group has multiple two-fold screw axes. In the case of MnGaGe, crystallizing in $P4/nmm$ space group possesses two pairs of nodal surface on the $k_x = \pm\pi$ and $k_y = \pm\pi$ planes due to the presence of two-fold rotation symmetries, $\mathcal{S}_{2x}$ and $\mathcal{S}_{2y}$. Although this paper only discusses the $k_y = \pi$ plane, the ($\mathcal{S}_{4z}$) symmetry allows for the observation of equivalent states on the $k_y = -\pi$ and $k_x = \pm\pi$ planes as well [72]. The spin-polarized nodal surface and their response to magnetization directions have been reported earlier in the magnetic compounds $CsCrI_3$ [39] and $LiTiO_2$ [40] which is extremely uncommon.

4.2. Nodal line features and Weyl nodes

A careful introspection of the band structure depicted in figure 3(a), several band crossings could be seen in the spin-down channel. Here, we focus on the dispersion formed by the band crossings between Γ–X and R–Z which is at 0.28 eV and 0.31 eV away from the E_F. The band structure

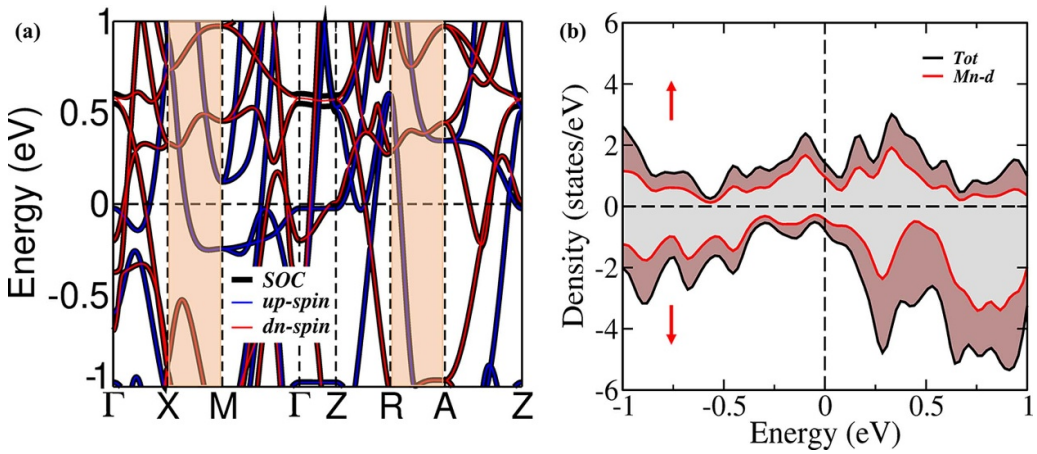

Figure 3. (a) The electronic band structure of MnGaGe with the shaded region highlighting the doubly degenerate bands along *X*–*M* and *R*–*A* with and without SOC. (b) The spin-resolved density of states with (↑) and (↓) arrows pointing to spin-up and spin-down.

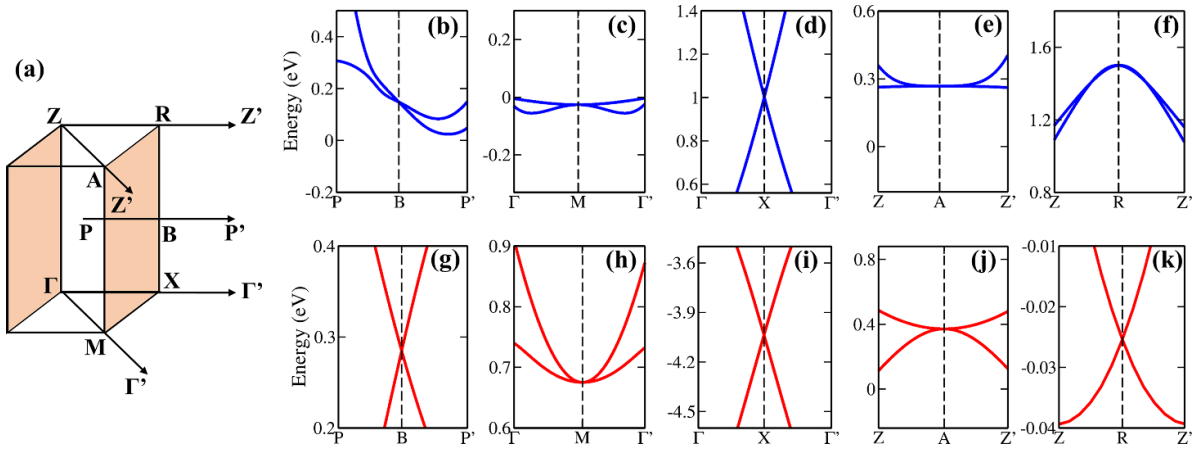

Figure 4. (a) The symmetry paths normal to $k_y = \pi$ plane in the BZ. The calculated band dispersion along the symmetry paths for the spin-up channel in (b)–(f) and spin-down channel in (g)–(k).

of MnGaGe along the path Γ–X–R–Z–Γ ($k_x = 0$ plane) in the spin-down channel along with the orbital projections of contributing Mn-d states is given in figure 6(a). It is found that the band hybridization forms the nodal line-like dispersion amid Mn-d_{yz} and Mn-d_{z^2} states. For further confirmation, several band pathways have been chosen as shown in figure 6(b) between Γ–X and R–Z and computed the dispersion. A similar kind of band crossing is observed along all the pathways as illustrated in figure 6(c). The inclusion of SOC along [001] direction lifts the degeneracy and makes the nodal line gaped with band inversion as shown in the insets in figure 6(a), indicating the non-trivial nature. The magnetization along the [001] direction breaks the screw-rotation axis $\mathcal{S}_{2x}$ and $\mathcal{S}_{2y}$, the glide mirror symmetry $\mathcal{G}_x$ and $\mathcal{G}_y$, and the rotation symmetry $\mathcal{C}_{4x}$ and $\mathcal{C}_{4y}$.

Now, let us look into the interesting crossing points close to E_F formed by the band hybridization between the spin-up and spin-down channel along the path Γ–X–M–Γ (i.e. $k_z = 0$ plane) as depicted in figure 7(a). The iso-energy band crossings amid Γ–X and M–Γ are found to be at -0.05 eV away from the E_F. It is found that the band hybridization between the Mn-d_{xy} and Mn-d_{z^2} states leads to the formation of the nodal ring-like dispersion in the $k_z = 0$ plane as illustrated by the orbital projected bands in figure 7(b).

Inclusion of SOC along the [001] direction does not considerably alter the band profile but lifts degeneracy and causes band inversion as exhibited in the insets in figure 7(b). The iso-energy band crossings between Γ–X and M–Γ lead to the nodal ring-like dispersion which gets gaped in the presence of SOC as depicted by the gap plane calculation in figure 8(a). There have been previous reports of such small gap openings along the nodal ring in other systems like ZrSiS [73, 74], Cu_3PdN [75], TiB_2 [76].

The band inversion taking place in the presence of SOC serves as an indication of the non-trivial nature. To further support this, Berry phase calculation defining a closed loop encircling the nodal ring is performed and turned out to be $-\pi$, confirming the topological non-triviality [9, 77]. Huge BC is usually generated by non-trivial band topologies. Figure 8(b) demonstrates the positive z component of the BC, $\Omega_z(k)$ in the corresponding $k_z = 0$ plane for the magnetization along [001] direction. As MnGaGe adopts FM ordering, the magnetic ground state lacks time-reversal symmetry and is anticipated

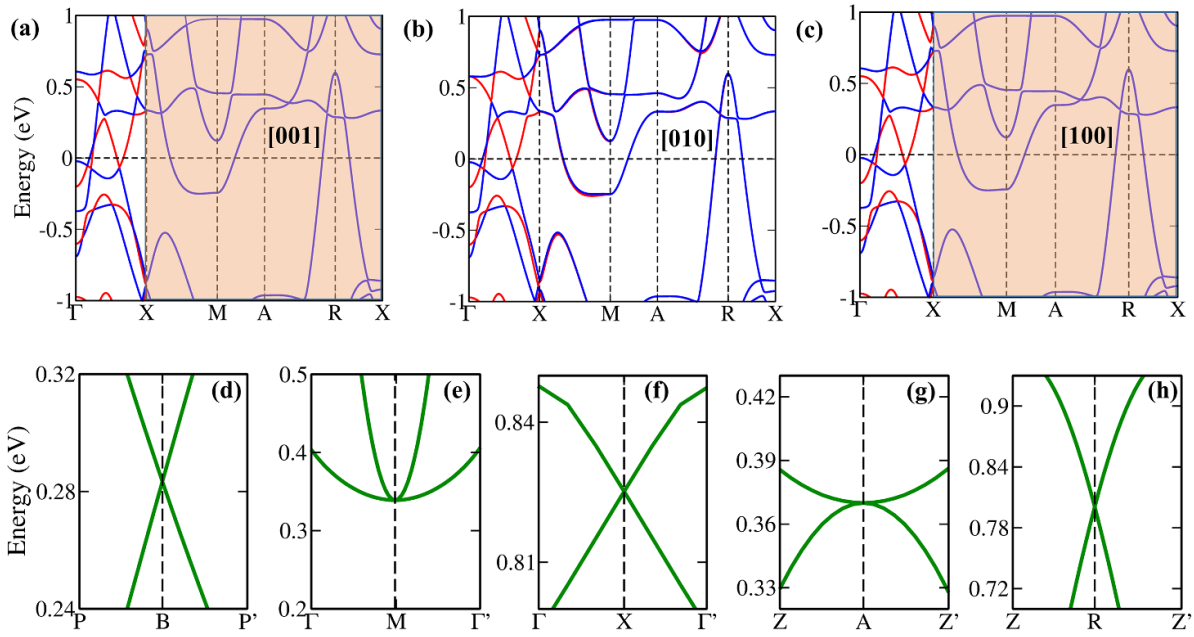

Figure 5. (a)–(c) Band dispersion along the k-path Γ–X–M–A–R–X for different magnetization directions. The shaded region illustrates the transition of non-degenerate red and blue bands along the Γ–X to becoming doubly degenerate along the Γ–X–M–A–R–X path. (d)–(h) The calculated band dispersion along the symmetry paths with the inclusion of SOC along [001] direction.

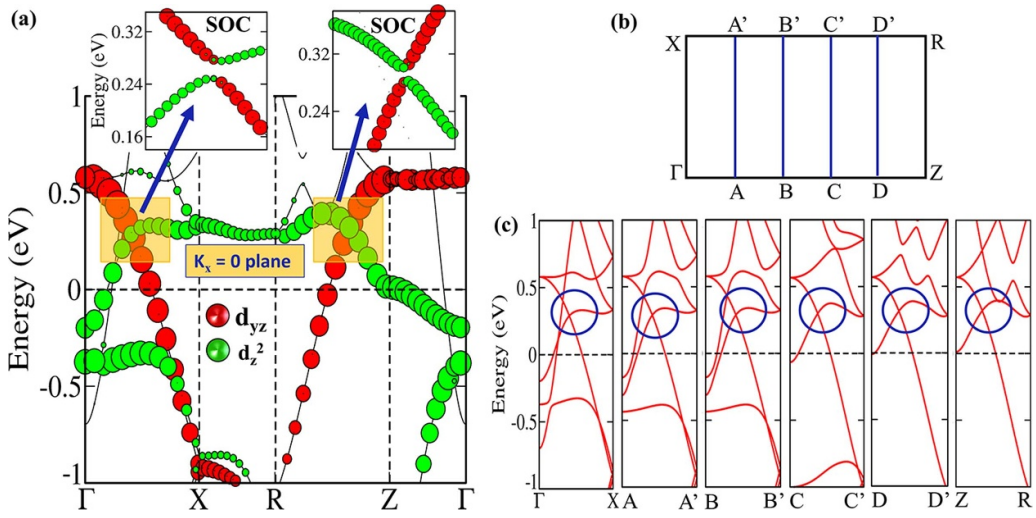

Figure 6. (a) Band dispersion in the spin-down channel with orbital projections along Γ–X–R–Z–Γ ($k_x = 0$ plane), without and with the inclusion of SOC indicating the band inversion. (b), (c) Nodal line illustration along the chosen band pathways between Γ–X and R–Z.

to have Weyl points in the presence of SOC in the BZ. The magnetization along [001] direction preserves the inversion symmetry, glide mirror $\mathcal{G}_z$, and screw-rotation $\mathcal{S}_{2z}$ and rotation symmetry $\mathcal{C}_{4z}$. Four pairs of Weyl nodes are found as tabulated with opposite chiralities in table 3. Weyl nodes are marked in the BZ and their band dispersion is depicted in figures 8(c) and (d). These eight Weyl nodes have a cumulative total topological charge of zero as per Nielsen–Ninomiya no-go theorem [78]. The Weyl node, a magnetic monopole with a topological charge, is a source or sink of the BC flux in momentum space. This flux is defined as wiring a sphere encircling the Weyl point with a value of either $+1$ or -1, according to the chirality of the Weyl fermion [79]. The Chern number corresponding to the Weyl node $W^{\pm}_{i=1,2,3,4}$ is given by $\mathcal{C} = \pm 1$ [80]. There have been previous reports on the existence of Weyl semimetal phases protected by two-fold rotation symmetry within tetragonal systems. These phases have been observed in materials possessing inversion symmetry, such as Cu-based chalcogenides [81], and in those lacking inversion symmetry, exemplified by ABX_2 family of chalcopyrites (A = Cu, Ag, Au, Zn, B = TI, Pb, X = Se, Te, As) [82]. Additionally, Weyl semimetal phases have been identified in structures like HgTe/HgSe (001) [83] and HgTe/MnTe (001) [84] superlattices.

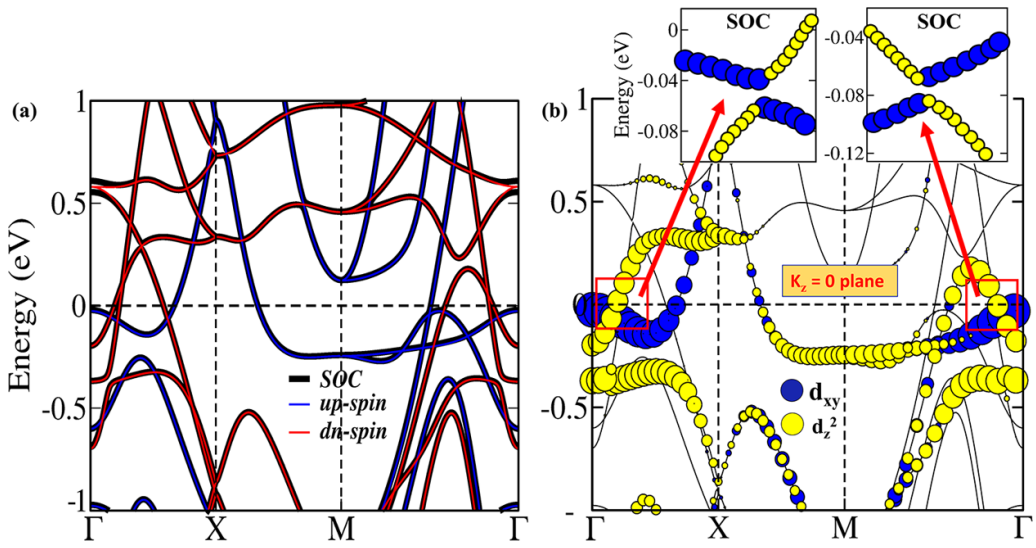

Figure 7. (a) Band structure along the path Γ–X–M–Γ (i.e. $k_z = 0$ plane) depicting the interesting crossing points in the red box. (b) The orbital projected bands without and with the inclusion of SOC illustrate the band inversion.

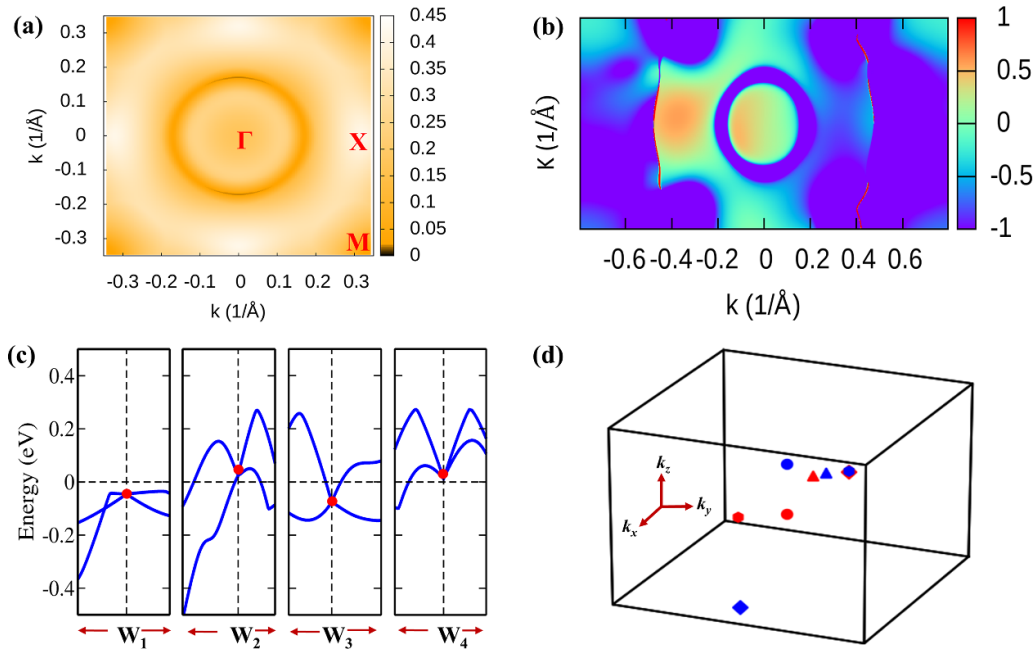

Figure 8. (a) Nodal ring-like dispersion depicted by the gap plane calculation in the presence of SOC. (b) The positive z component of the BC, $\Omega_z(k)$ for the magnetization along [001] direction. (c) and (d) Band dispersion around the four positive chiral Weyl nodes and the Weyl node locus in the BZ are shown, with red and blue denoting the positive and negative nodes, respectively.

4.3. Anomalous Hall conductivity

The topological phase of a material can be ascertained via band structure properties, such as the BC, which may provide fascinating anomalous transport behavior. In terms of BC and AHC, control is obtained by tinkering with band structures and symmetries, which are independent of finite magnetization values. In combination with SOC, the magnetization direction [001] affects how the system's symmetry is broken, leading to the induction of BC, $\Omega_z(k)$ close to E_F calculated from MLWF using the Kubo-formula [85]

$$\Omega_n^z(\boldsymbol{k}) = -2\mathrm{Im}\sum_{m\neq n}\frac{\langle\psi_{n\boldsymbol{k}} \mid v_x \mid \psi_{m\boldsymbol{k}}\rangle\langle\psi_{m\boldsymbol{k}} \mid v_y \mid \psi_{n\boldsymbol{k}}\rangle}{\left[E_m(\boldsymbol{k}) - E_n(\boldsymbol{k})\right]^2}, \qquad (2)$$

where $E_n(\boldsymbol{k})$ is the eigenvalue of the nth eigenstate $\psi_{n\boldsymbol{k}}$, $\boldsymbol{k}$ is the wave vector, n is the index of the occupied bands, and v's are

Table 3. Weyl point coordinates in the BZ and their respective chiralities, where $W_i^{\pm}$ represents the ith Weyl point with the chirality ± 1.

Weyl points	Coordinates (k_x, k_y,k_z)	Chirality
W_1^+	(−0.087, 0.087, −0.143)	+1
W_1^-	(−0.087, 0.087, 0.143)	−1
W_2^+	(0.438, 0.018, 0.171)	+1
W_2^-	(−0.438, 0.018, −0.171)	−1
W_3^+	(−0.052, 0.487, −0.016)	+1
W_3^-	(0.055, 0.487, 0.012)	−1
W_4^+	(−0.444, −0.000, −0.179)	+1
W_4^-	(0.444, −0.000, 0.178)	−1

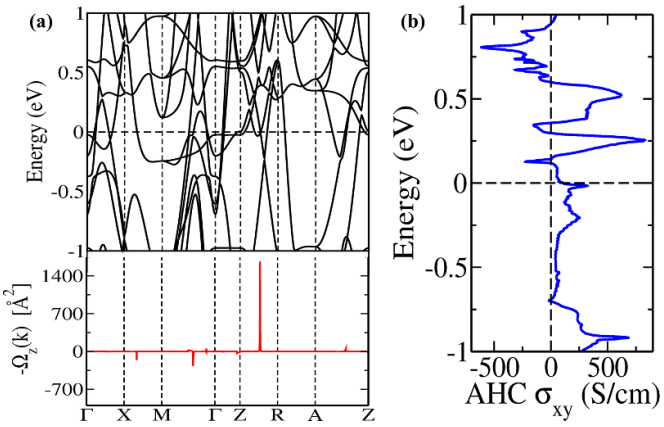

Figure 9. (a) Band structure of MnGaGe in the presence of SOC along with the non-vanishing BC along the high-symmetry path in (a) and the computed AHC plot in (b).

the velocity operators. With the principle transport parameter σ_{xy}, AHC is extracted from BC

$$\sigma_{xy} = -\frac{e^2}{\hbar}\int_{BZ}\frac{\mathrm{d}^3\boldsymbol{k}}{(2\pi)^3}\sum_n f(\boldsymbol{k})\,\Omega_n^z(\boldsymbol{k})\,, \tag{3}$$

$f(\boldsymbol{k})$ is the Fermi–Dirac distribution function. The non-vanishing BC caused by the inclusion of SOC creates gap at the crossing points leading to peaks and small valleys in the corresponding band path as shown in figure 9(a). The calculated value of AHC at the E_F is found to be 112.5 S cm^{-1}, which then increases to a value of −216.5 S cm^{-1} at 0.1 eV and then attains a maximum value of 827.9 S cm^{-1} at 0.25 eV as illustrated in figure 9(b). These values are found to be comparable with the values of other magnetic compounds like MnAlGe [43], ZrMnP, and HfMnP [86].

5. Phononic band structure

MnGaGe has a six-atom unit cell with 18 phonon modes: 3 acoustic and 15 optical. Phonon dispersion from 0 to 9 THz is presented in figure 10(a), ensuring the dynamical stability with no imaginary modes. Multiple band crossings in various frequency ranges indicate topological features which will be discussed in detail below.

5.1. Nodal surface phonons

An extensive investigation of the phonon spectra exposes the existence of doubly degenerate band dispersion along X–M and R–A, which forms a 2D surface along the k-path X–M–A–R–X, which is located on the $k_y = \pi$ plane in the BZ as depicted in figure 10(b). The coexistence of time-reversal symmetry ($\mathcal{T}$) and non-symmorphic two-fold screw-rotational symmetry ($\mathcal{S}_{2i}$) protects the class-II type of nodal surface present in the phononic spectra [72]. The two-fold screw-rotation symmetry $\mathcal{S}_{2y}$, involving $\mathcal{C}_2$ rotational and [010] translational symmetries, preserves the nodal surface on $k_y = \pi$. The symmetry conditions discussed in section 4.1 for the electronic spectra without SOC apply equally to phonons. Band dispersions along symmetry pathways in figures 10(c)–(g) reveal nodal surface at $k_y = \pi$ plane, where Kramer's two-fold degeneracy is evident due to prevailing symmetry. The presence of $\mathcal{S}_{4z}$ symmetry also leads to comparable nodal surface states on the $k_y = -\pi$ and $k_x = \pm\pi$ planes [72].

5.2. Nodal line features

The phonon dispersion along the path Γ–X–M–Γ ($k_z = 0$ plane) exhibits some intriguing band crossings between Γ–X and M–Γ at the distinct frequency ranges 6.98 THz and 7.50 THz hosting nodal line features. These crossings are formed by the symmetry states having opposite parity eigenvalues and their protection against the band hybridization is ensured by glide mirror symmetry $\mathcal{G}_z$. The band crossings are represented by the symmetry states A_{2u} and A_{1g} at the frequency of 6.98 THz and by A_{2u}, E_g and A_{1g} at the frequency of 7.50 THz as shown in figure 11(a).

The phonon surface state computations on the (001) surface confirm nodal line features as depicted figure 11(b). Additionally, isofrequency arc plots at 6.98 THz and 7.50 THz depict the presence of two nodal rings in figures 11(c) and (d). Berry phase calculations through a loop in the k-space encircling a point on the nodal ring, yield a value of π confirming the non-trivial topological nature.

6. Quantum transport in MnGaGe monolayer

This section focuses on the quantum transport characteristics of the MnGaGe monolayer (001 plane). The crystal lattice structure of the monolayer is depicted in figure 12(a), and its dynamic stability is ensured by the positive phonon dispersion curve, as illustrated in figure 12(b). To gain a deeper understanding of the magnetic and transport characteristics of the monolayer, AHC has been calculated. This property holds significant value in quantum transport devices, which involve precise manipulation and regulation of electronic transport at

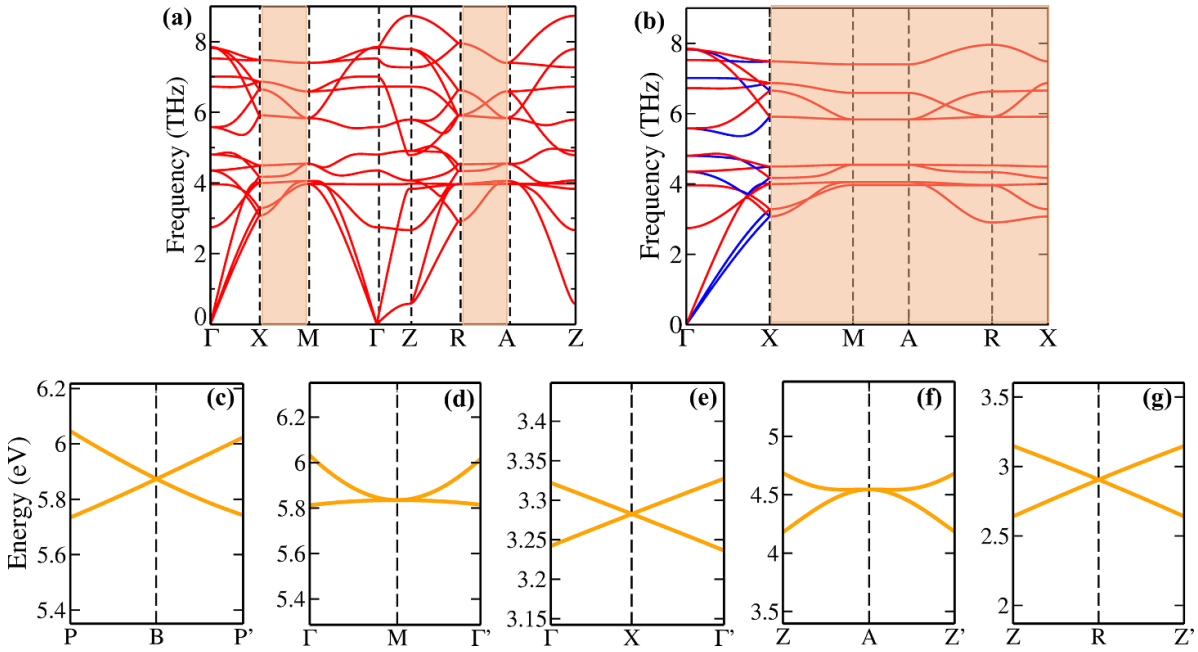

Figure 10. (a) Phonon dispersion of MnGaGe highlighting the doubly degenerate bands along *X*–*M* and *R*–*A*. (b) Dispersion along the path Γ–*X*–*M*–*A*–*R*–*X* projecting the 2D surface along *X*–*M*–*A*–*R*–*X*. The shaded region illustrates the transition of non-degenerate red and blue bands along the Γ–*X* to becoming doubly degenerate along the Γ–*X*–*M*–*A*–*R*–*X* path. (c)–(g) The calculated band profile along the various symmetry paths.

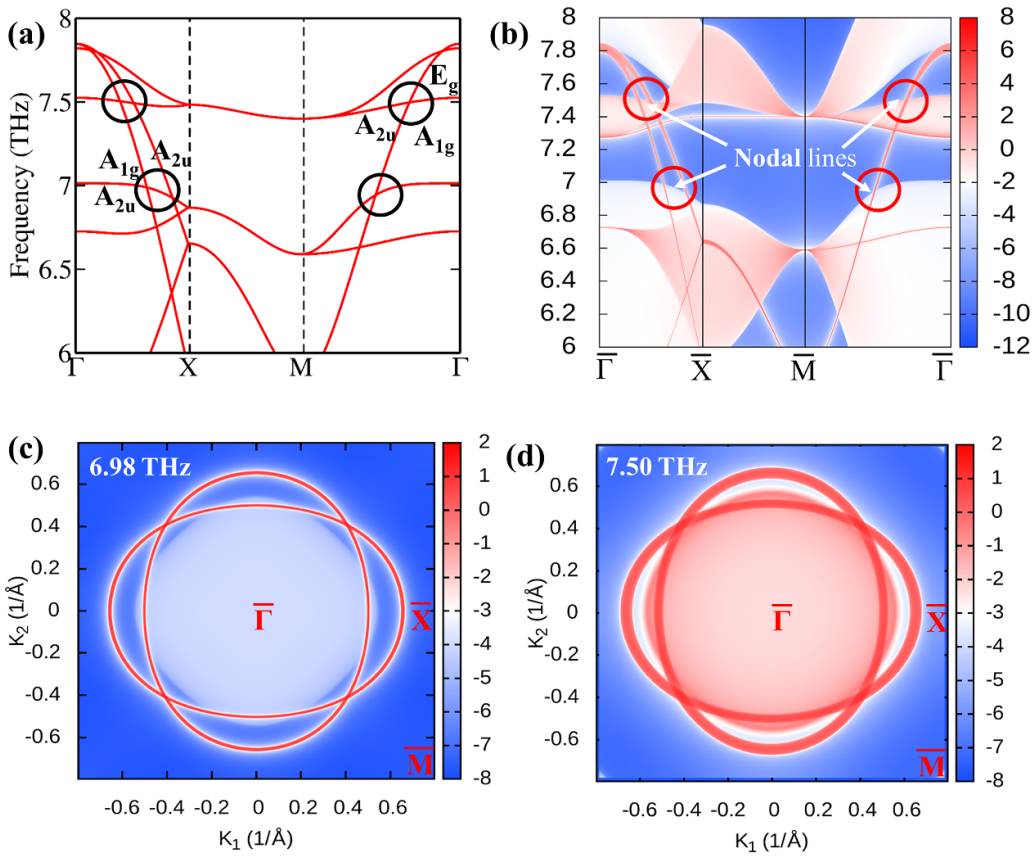

Figure 11. (a) The phonon band structure in the $k_z = 0$ illustrating the nodal crossings between symmetry states with opposite parity eigenvalues. (b) Phonon surface states along the (001) surface. (c) and (d) The isofrequency arc state at a frequency of $\omega = 6.98$ THz and $\omega = 7.50$ THz along the (001) surface.

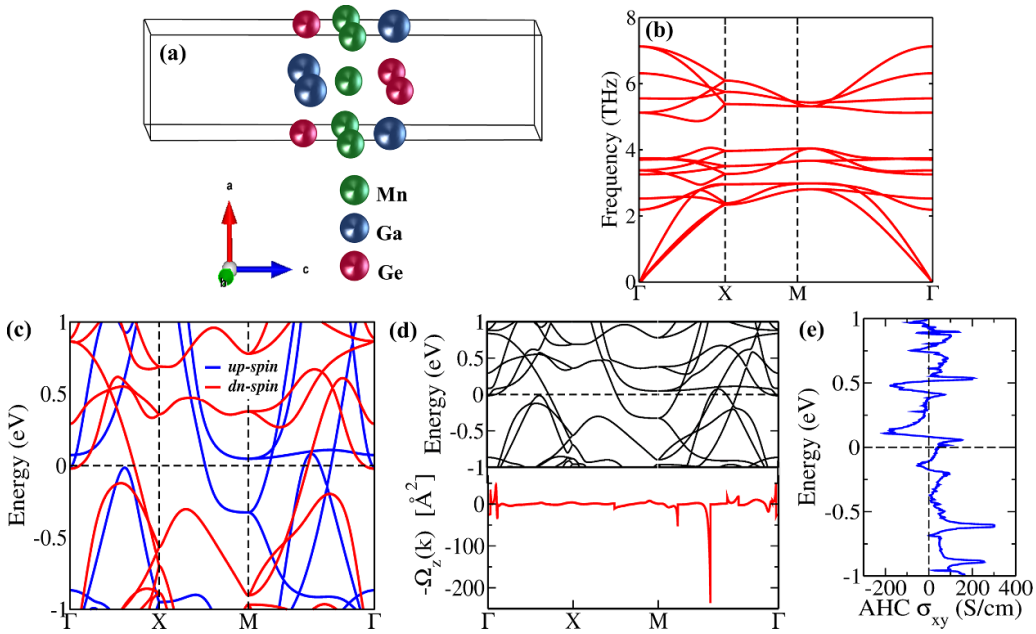

Figure 12. (a) The lattice structure of MnGaGe monolayer (001). (b) Phonon dispersion. (c) and (d) The band structure without and with SOC featuring BC at high symmetry points. (e) The AHC plot.

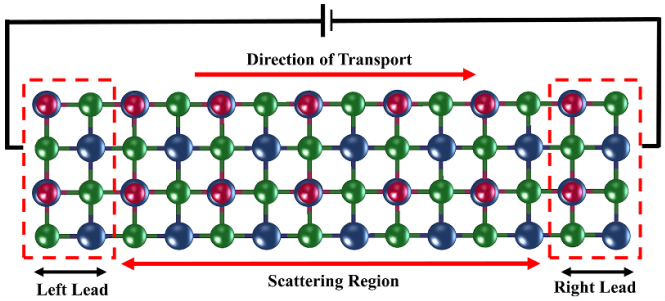

Figure 13. A schematic visualization of a two-terminal device.

the nanoscale level. AHC, in essence, reflects the material's capacity to facilitate the flow of an electrical current perpendicular to a magnetic field applied to it. This arises from the interplay between the electrons' spin and their orbital motion, which gives rise to a distinctive BC in momentum space.

The electronic band structure of monolayer without and including SOC leading to BC trajectory has been depicted in figures 12(c) and (d) along with the corresponding AHC plot in figure 12(e) with a value of 62.4 S cm^{-1} at the E_F, which then increases to a value of 157.4 S cm^{-1} at 0.06 eV and then attains a maximum value of 308.2 S cm^{-1} at -0.6 eV.

The monolayer has been transformed into a two-terminal device model comprising 84 atoms arranged in seven primitive cells. To facilitate transport calculations, the device is partitioned into three sections: a central scattering region with dimensions $1 \times 2 \times 5$ (60 atoms) flanked by two infinitely long semi-infinite electrodes (left and right) with dimensions $1 \times 2 \times 1$ (12 atoms) as illustrated in figure 13. To assess the current sensitivity of the proposed device, we utilized an equivalent transport theory [65] to compute its *I–V* characteristics.

The obtained *I–V* curve displayed a linear increase in current with voltage, indicating the metallic nature of the compound, as depicted in figure 14(a). The conductance value was determined to be 1.66×10^{-4} S from figure 14(a), where a steeper slope corresponded to a higher conductance value. The relationship between conductance and transmission was explained in terms of the Landauer–Büttiker formalism [66], which describes the quantum transport of electrons. This formalism suggests that the conductance of a conductor is dependent on the DOS and the transmission probability of the electrons.

The quantum conductance is expressed as $G = \frac{2e^2}{h}T(E)$, where e is the elementary charge, h is Planck's constant, and $T(E)$ is the transmission probability of electrons at E_F. The value of quantum conductance obtained is 7.7×10^{-4} S. Notably, conductance bears a direct relationship with the transmission probability of electrons, indicating that materials or devices characterized by a greater transmission probability will manifest a higher conductance, while those featuring a lower transmission probability will correspondingly exhibit lower conductance. Figure 14(b) showcases an integer

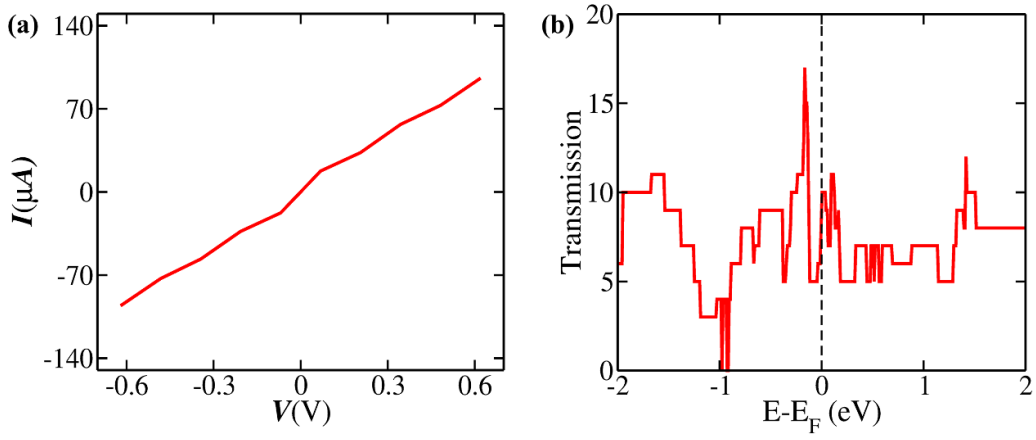

Figure 14. (a) The current–voltage (I–V) characteristics. (b) The transmission spectrum at zero-bias voltage.

sequence of transmission steps, denoting the number of open channels and revealing an upsurge in transmission in the vicinity of E_F under zero bias.

7. Discussion and conclusion

The imperative to gain a deeper understanding and identify tangible materials that harbor the coexistence of topological electrons and phonons has become a critical research priority. The demand for these quasiparticles stems from their scientific and practical significance, making the pursuit of such materials highly valuable. From the above discussions, it is found that investigated compounds possess both nodal surface and nodal line features in their electronic as well as phononic spectra. These aspects would exhibit independent behavior and contribute to physical attributes differently. For example, the transport parameter σ_{xy} would be contributed by the nodal line fermions in the $k_z = 0$ plane. It is also anticipated that the two types of fermions will have distinct signatures in the magnetic quantum oscillations [38]. The presence of a nodal ring-like dispersion gives rise to closed cyclotron orbits when subjected to a magnetic field, leading to quantum oscillations reminiscent of de Haas–van Alphen oscillations [87]. The NS fermions, however, are more likely to form open orbits and have no effect on the oscillations [88]. Furthermore, topological phonons are implicated in electron–phonon interaction [89], unusual heat transfer [90], and phonon diodes [91]. Topological phonons also exhibit anomalous transport behavior, such as the anomalous phonon Hall effect, in accordance with electrons [92, 93].

The connection between AHC and device efficiency lies in the impact of AHC on the electronic transport properties of the device material. Specifically, the AHC influences the material's resistance, which can have significant implications for the power consumption and overall efficiency of the device. A material with a high positive AHC, such as a ferromagnet, can be utilized in magnetic sensors, where changes in the magnetic field are detected by monitoring the sensor's resistance changes. Thus, understanding the AHC of material is crucial in designing and optimizing quantum transport devices with desired electronic and magnetic properties.

In conclusion, we propose the intermetallic compounds MnGaGe and MnZnSb with the coexistence of exquisite topological properties in the electronic and phononic states by first-principles calculations and symmetry analysis. These compounds are found to be FM with their ground state magnetization along [001] direction. In the electronic and phononic spectra, the nodal surface on the $k_y = \pi$ plane is protected by the combination of time-reversal symmetry and nonsymmorphic two-fold screw-rotation symmetry. In the electronic spectra, spin-polarized nodal surface in both the spin channels and their robustness to magnetic ground state polarization have been discussed, which is quite rare. Nodal line features in both the quasiparticle spectra have been analyzed and further Berry phase calculation confirms their topological non-triviality. An ideal framework for developing a BC-driven AHC is provided by the inclusion of SOC in the electron spectra, which results in fascinating transport features. Additionally, the monolayer has been incorporated into a two-terminal device model to investigate nanoscale properties. Integrating topological materials into nanoscale devices shows significant potential for advancing innovative electronics.

Data availability statement

The data cannot be made publicly available upon publication because they are not available in a format that is sufficiently accessible or reusable by other researchers. The data that support the findings of this study are available upon reasonable request from the authors.

Acknowledgments

The authors gratefully acknowledge the support and resources provided by IIT Hyderabad and the National Supercomputing Mission through the 'PARAM SEVA' implementation by CDAC for computational resources. They also extend their gratitude to the DST-SERB project with sanction no.

CRG/2022/005228 for the financial support that facilitated this research. ACV acknowledges IIT Hyderabad for the research fellowship, and VK extends appreciation for the financial support received from DST-FIST (SR/FST/PSI-215/2016).

ORCID iDs

Anusree C V https://orcid.org/0009-0006-2702-8961
Sonali S Pradhan https://orcid.org/0009-0003-7722-3720
V Kanchana https://orcid.org/0000-0003-1575-9936

References

[1] Qi X-L and Zhang S-C 2011 *Rev. Mod. Phys.* **83** 1057–110
[2] Yan B and Felser C 2017 *Ann. Rev. Condens. Matter Phys.* **8** 337–54
[3] Chiu C-K, Teo J C,Y, Schnyder A P and Ryu S 2016 *Rev. Mod. Phys.* **88** 035005
[4] Weng H, Fang C, Fang Z, Bernevig B A and Dai X 2015 *Phys. Rev.* X **5** 011029
[5] Wan X, Turner A M, Vishwanath A and Savrasov S Y 2011 *Phys. Rev.* B **83** 205101
[6] Wang Z, Weng H, Wu Q, Dai X and Fang Z 2013 *Phys. Rev.* B **88** 125427
[7] Wang Z, Sun Y, Chen X-Q, Franchini C, Xu G, Weng H, Dai X and Fang Z 2012 *Phys. Rev.* B **85** 195320
[8] Huang H, Liu J, Vanderbilt D and Duan W 2016 *Phys. Rev.* B **93** 201114
[9] Fang C, Weng H, Dai X and Fang Z 2016 *Chin. Phys.* B **25** 117106
[10] Kim Y, Wieder B J, Kane C L and Rappe A M 2015 *Phys. Rev. Lett.* **115** 036806
[11] Hyart T, Ojajärvi R and Heikkilä T T 2018 *J. Low Temp. Phys.* **191** 35–48
[12] Bradlyn B, Cano J, Wang Z, Vergniory M G, Felser C, Cava R J and Bernevig B A 2016 *Science* **353** aaf5037
[13] Nie S, Bernevig B A and Wang Z 2021 *Phys. Rev. Res.* **3** L012028
[14] Khan M R, Bu K and Wang J-T 2021 *Phys. Chem. Chem. Phys.* **23** 25944–50
[15] Weng H, Liang Y, Xu Q, Yu R, Fang Z, Dai X and Kawazoe Y 2015 *Phys. Rev.* B **92** 045108
[16] Wang J-T, Weng H, Nie S, Fang Z, Kawazoe Y and Chen C 2016 *Phys. Rev. Lett.* **116** 195501
[17] Khan M R, Bu K and Wang J-T 2022 *New J. Phys.* **24** 043007
[18] Wang J-T, Chen C and Kawazoe Y 2018 *Phys. Rev.* B **97** 245147
[19] He H, Qiu C, Ye L, Cai X, Fan X, Ke M, Zhang F and Liu Z 2018 *Nature* **560** 61–64
[20] Süsstrunk R and Huber S D 2015 *Science* **349** 47–50
[21] Prodan E and Prodan C 2009 *Phys. Rev. Lett.* **103** 248101
[22] Zhang T, Song Z, Alexandradinata A, Weng H, Fang C, Lu L and Fang Z 2018 *Phys. Rev. Lett.* **120** 016401
[23] Li J, Liu J, Baronett S A, Liu M, Wang L, Li R, Chen Y, Li D, Zhu Q and Chen X Q 2021 *Nat. Commun.* **12** 1–12
[24] Chen Z, Wang R, Xia B, Zheng B, Jin Y, Zhao Y-J and Xu H 2021 *Phys. Rev. Lett.* **126** 185301
[25] Jin Y, Wang R and Xu H 2018 *Nano Lett.* **18** 7755–60
[26] Wang R, Xia B, Chen Z, Zheng B, Zhao Y and Xu H 2020 *Phys. Rev. Lett.* **124** 105303
[27] Huang Z, Chen Z, Zheng B and Xu H 2020 *npj Comput. Mater.* **6** 1–7
[28] Zheng B, Zhan F, Wu X, Wang R and Fan J 2021 *Phys. Rev.* B **104** L060301
[29] Liu Q-B, Wang Z-Q and Fu H-H 2021 *Phys. Rev.* B **104** L041405
[30] Xie C, Yuan H, Liu Y, Wang X and Zhang G 2021 *Phys. Rev.* B **104** 134303
[31] Wang J, Yuan H, Yu Z-M, Zhang Z and Wang X 2021 *Phys. Rev. Mater.* **5** 124203
[32] Zheng B, Xia B, Wang R, Chen Z, Zhao J, Zhao Y and Xu H 2020 *Phys. Rev.* B **101** 100303
[33] Li J, Xie Q, Liu J, Li R, Liu M, Wang L, Li D, Li Y and Chen X-Q 2020 *Phys. Rev.* B **101** 024301
[34] Zhong C, Chen Y, Xie Y, Yang S A, Cohen M L and Zhang S 2016 *Nanoscale* **8** 7232–9
[35] Liang Q-F, Zhou J, Yu R, Wang Z and Weng H 2016 *Phys. Rev.* B **93** 085427
[36] Wu W, Liu Y, Li S, Zhong C, Yu Z-M, Sheng X-L, Zhao Y X and Yang S A 2018 *Phys. Rev.* B **97** 115125
[37] Khan M R, Bu K, Wang J-T and Chen C 2022 *Phys. Rev.* B **105** 245152
[38] Zhang X, Yu Z-M, Zhu Z, Wu W, Wang S-S, Sheng X-L and Yang S A 2018 *Phys. Rev.* B **97** 235150
[39] He T, Liu Y, Tian L, Zhang X, Meng W, Dai X and Liu G 2021 *Phys. Rev.* B **103** 085135
[40] Yang T, Jin L, Liu Y, Zhang X and Wang X 2021 *Phys. Rev.* B **103** 235140
[41] Kou L, Tang C, Guo W and Chen C 2011 *ACS Nano* **5** 1012–7
[42] Hsu C-C, Teague M, Wang J-Q and Yeh N-C 2020 *Sci. Adv.* **6** eaat9488
[43] Guin S N *et al* 2021 *Adv. Mater.* **33** 2006301
[44] Jin Y J, Wang R, Chen Z J, Zhao J Z, Zhao Y J and Xu H 2017 *Phys. Rev.* B **96** 201102
[45] Tang P, Zhou Q, Xu G and Zhang S-C 2016 *Nat. Phys.* **12** 1100–4
[46] Anusree C V, Rudenko A N, Manivel Raja M and Kanchana V 2022 *Comput. Mater. Sci.* **213** 111625
[47] Rambabu P, Anusree C V, Manivel Raja M and Kanchana V 2022 *J. Magn. Magn. Mater.* **562** 169766
[48] Watts L, Haidar E-A and Stampfl C 2022 *J. Phys. Chem.* C **126** 15397–404
[49] Rani R, Yoshimura A, Das S, Sahoo M R, Kundu A, Sahu K K, Meunier V, Nayak S K, Koratkar N and Hazra K S 2020 *ACS Nano* **14** 6258–68
[50] Novoselov K S, Geim A K, Morozov S V, Jiang D, Katsnelson M I, Grigorieva I V, Dubonos S and Firsov A A 2005 *Nature* **438** 197–200
[51] Raval D, Gupta S K, Gajjar P and Ahuja R 2022 *Sci. Rep.* **12** 2964
[52] Sahoo M R, Nayak S K and Pradhan K 2022 *J. Phys. Chem.* C **126** 4638–46
[53] Sahoo M R, Kushwaha A K, Pati R, Ajayan P and Nayak S K 2019 *J. Magn. Magn. Mater.* **484** 462–71
[54] Kresse G and Furthmüller J 1996 *Phys. Rev.* B **54** 11169–86
[55] Kresse G and Joubert D 1999 *Phys. Rev.* B **59** 1758–75
[56] Perdew J P, Burke K and Ernzerhof M 1996 *Phys. Rev. Lett.* **77** 3865–8
[57] Togo A and Tanaka I 2015 *Scr. Mater.* **108** 1–5
[58] Marzari N and Vanderbilt D 1997 *Phys. Rev.* B **56** 12847–65
[59] Marzari N, Mostofi A A, Yates J R, Souza I and Vanderbilt D 2012 *Rev. Mod. Phys.* **84** 1419–75
[60] Mostofi A A, Yates J R, Lee Y-S, Souza I, Vanderbilt D and Marzari N 2008 *Comput. Phys. Commun.* **178** 685–99
[61] Nagaosa N, Sinova J, Onoda S, MacDonald A H and Ong N P 2010 *Rev. Mod. Phys.* **82** 1539–92
[62] Xiao D, Chang M-C and Niu Q 2010 *Rev. Mod. Phys.* **82** 1959–2007
[63] Wu Q, Zhang S, Song H-F, Troyer M and Soluyanov A A 2018 *Comput. Phys. Commun.* **224** 405–16
[64] Soler J M, Artacho E, Gale J D, García A, Junquera J, Ordejón P and Sánchez-Portal D 2002 *J. Phys.: Condens. Matter* **14** 2745–79
[65] Ferrer J *et al* 2014 *New J. Phys.* **16** 093029

[66] Brandbyge M, Mozos J-L, Ordejón P, Taylor J and Stokbro K 2002 *Phys. Rev.* B **65** 165401
[67] Kanomata T, Endo H, Mori S, Okajima H, Hihara T, Sumiyama K, Kaneko T and Suzuki K 1995 *J. Magn. Magn. Mater.* **140–4** 133–4
[68] Shibata K, Watanabe H, Yamauchi H and Shinohara T 1973 *J. Phys. Soc. Japan* **35** 448–51
[69] Mohn P and Schwarz K 1996 *J. Magn. Magn. Mater.* **157–8** 721–2
[70] Kanomata T, Endo H, Ichi Mori S, Sakatsume S, Yoshida H and Kaneko T 1993 *Jpn. J. Appl. Phys.* **32** 269
[71] Motizuki K, Korenari T and Shirai M 1992 *J. Magn. Magn. Mater.* **104–7** 1923–4
[72] Xie C, Yuan H, Liu Y and Wang X 2022 *Phys. Rev.* B **105** 054307
[73] Hosen M M *et al* 2017 *Phys. Rev.* B **95** 161101
[74] Schoop L M, Ali M N, Straßer C, Topp A, Varykhalov A, Marchenko D, Duppel V, Parkin S S P, Lotsch B V and Ast C R 2016 *Nat. Commun.* **7** 11335
[75] Yu R, Weng H, Fang Z, Dai X and Hu X 2015 *Phys. Rev. Lett.* **115** 036807
[76] Liu Z *et al* 2018 *Phys. Rev.* X **8** 031044
[77] Huang H, Jiang W, Jin K-H and Liu F 2018 *Phys. Rev.* B **98** 045131
[78] Nielsen H and Ninomiya M 1981 *Phys. Lett.* B **105** 219–23
[79] Li F, Huang X, Lu J, Ma J and Liu Z 2018 *Nat. Phys.* **14** 30–4
[80] Hsu C-H, Sreeparvathy P C, Barman C K, Chuang F-C and Alam A 2021 *Phys. Rev.* B **103** 195143
[81] Qian Y, Gao J, Song Z, Nie S, Wang Z, Weng H and Fang Z 2020 *Phys. Rev.* B **101** 155143
[82] Ruan J, Jian S-K, Zhang D, Yao H, Zhang H, Zhang S-C and Xing D 2016 *Phys. Rev. Lett.* **116** 226801
[83] Islam R, Ghosh B, Cuono G, Lau A, Brzezicki W, Bansil A, Agarwal A, Singh B, Dietl T and Autieri C 2022 *Phys. Rev. Res.* **4** 023114
[84] Islam R, Mardanya S, Lau A, Cuono G, Chang T-R, Singh B, Canali C M, Dietl T and Autieri C 2023 *Phys. Rev.* B **107** 125102
[85] Yao Y, Kleinman L, MacDonald A H, Sinova J, Jungwirth T, Wang D-S, Wang E and Niu Q 2004 *Phys. Rev. Lett.* **92** 037204
[86] Samathrakis I, Fortunato N, Singh H K, Shen C and Zhang H 2022 *J. Phys.: Condens. Matter* **35** 025703
[87] Zhang X, Yu Z-M, Lu Y, Sheng X-L, Yang H Y and Yang S A 2018 *Phys. Rev.* B **97** 125143
[88] Shoenberg D 1984 *Magnetic Oscillations in Metals* (*Cambridge Monographs on Physics*) (Cambridge University Press)
[89] Li J, Liu J, Baronett S, Liu M, Wang L, Li R, Chen Y, Li D, Zhu Q and Chen X 2021 *Nat. Commun.* **12** 1204
[90] Prodan E, Dobiszewski K, Kanwal A, Palmieri J and Prodan C 2017 *Nat. Commun.* **8** 14587
[91] Liu Y, Xu Y, Zhang S-C and Duan W 2017 *Phys. Rev.* B **96** 064106
[92] Sun K, Gao Z and Wang J-S 2021 *Phys. Rev.* B **103** 214301
[93] Qin T, Zhou J and Shi J 2012 *Phys. Rev.* B **86** 104305